Earth and Planetary Science Letters 482 (2018) 81–92

Contents lists available at ScienceDirect

Earth and Planetary Science Letters

www.elsevier.com/locate/epsl

Seismic behaviour of mountain belts controlled by plate convergence rate

Luca Dal Zilio [a], Ylona van Dinther [b], Taras V. Gerya [a], Casper C. Pranger [a]

[a] Geophysical Fluid Dynamics, ETH Zürich, Sonneggstrasse 5, 8092 Zürich, Switzerland
[b] Computational Seismology, ETH Zürich, Sonneggstrasse 5, 8092 Zürich, Switzerland

ARTICLE INFO

Article history:
Received 17 February 2017
Received in revised form 16 October 2017
Accepted 26 October 2017
Available online xxxx
Editor: R. Bendick

Keywords:
seismicity
mountain belts
convergence rate
Gutenberg–Richter law
numerical modelling

ABSTRACT

The relative contribution of tectonic and kinematic processes to seismic behaviour of mountain belts is still controversial. To understand the partitioning between these processes we developed a model that simulates both tectonic and seismic processes in a continental collision setting. These 2D seismo-thermo-mechanical (STM) models obtain a Gutenberg–Richter frequency–magnitude distribution due to spontaneous events occurring throughout the orogen. Our simulations suggest that both the corresponding slope (b value) and maximum earthquake magnitude ($M_{W\,max}$) correlate linearly with plate convergence rate. By analyzing 1D rheological profiles and isotherm depths we demonstrate that plate convergence rate controls the brittle strength through a rheological feedback with temperature and strain rate. Faster convergence leads to cooler temperatures and also results in more larger seismogenic domains, thereby increasing both $M_{W\,max}$ and the relative number of large earthquakes (decreasing b value). This mechanism also predicts a more seismogenic lower crust, which is confirmed by a transition from uni- to bi-modal hypocentre depth distributions in our models. This transition and a linear relation between convergence rate and b value and $M_{W\,max}$ is supported by our comparison of earthquakes recorded across the Alps, Apennines, Zagros and Himalaya. These results imply that deformation in the Alps occurs in a more ductile manner compared to the Himalayas, thereby reducing its seismic hazard. Furthermore, a second set of experiments with higher temperature and different orogenic architecture shows the same linear relation with convergence rate, suggesting that large-scale tectonic structure plays a subordinate role. We thus propose that plate convergence rate, which also controls the average differential stress of the orogen and its linear relation to the b value, is the first-order parameter controlling seismic hazard of mountain belts.

1. Introduction

Mountain building is the most spectacular manifestation of continental dynamics. The fact that mountain ranges are able to maintain their topography over tens of millions of years, is the evidence of how tectonic forces deform the continental crust (Avouac, 2015). Frequent earthquakes are the physical response of such crustal deformation, driven by convergence of continental plates.

Mitigating the impact of these earthquakes in mountain belts is crucial as part of these regions are densely populated. Moreover, understanding the partitioning of seismic and aseismic fault slip is central to seismotectonics, as it ultimately determines the seismic potential of faults. Although we cannot predict when and where the next earthquake will occur, we may forecast the maximum credible size and frequency of future events using the Gutenberg–Richter law (Gutenberg and Richter, 1944). This power law describes the frequency–magnitude distribution of earthquakes and its slope, the so-called b value, is commonly used to describe the relative occurrence of small and large events (e.g., Schorlemmer et al., 2005). From a physical mechanism perspective, local spatial variability of b and corresponding seismic hazard have been interpreted to relate to differences in the rheology of the crust (e.g., Pasquale et al., 2010), tectonic regime (e.g., Gulia and Wiemer, 2010; Doglioni et al., 2015), differential stress (e.g., Spada et al., 2013; Scholz, 2015), style-of-faulting (e.g., Schorlemmer et al., 2005), and degree of heterogeneity (e.g., Singh et al., 2009). On a larger regional scale, studies over the past decades have suggested that variations in seismicity of the mountain chains are related to variations in geologic structure (e.g., Bollinger et al., 2004; Grenerczy et al., 2005; Tatar et al., 2002). However, the preeminent physical parameter in controlling the seismic behaviour in orogenic mountain belts is still unclear.

E-mail address: luca.dalzilio@erdw.ethz.ch (L. Dal Zilio).

https://doi.org/10.1016/j.epsl.2017.10.053
0012-821X/

Mountain building processes acting on a time-scale of millions of years have been widely studied both using numerical models (e.g., Faccenda et al., 2008) and analogue experiments (e.g., Davis et al., 1983). These models have been used to investigate the effect of different physical characteristics on the evolving geometry and dynamics of a collisional margin. However, because of the relatively large computational time step (Δ_t =1000 yr), transient features and short-term processes, such as earthquakes, are not included. On the other hand, dynamic rupture simulations physically consistently model the propagation and arrest of a rupture for a set of unknown initial conditions—such as the stresses—and strength and the fault geometry (e.g., Dalguer, 2012). Alternatively, seismic cycle models simulate cycles of recurring interseismic and coseismic periods, either by kinematically defining slip or stress drop or by dramatically allowing rupture nucleation and propagation (e.g., Lapusta and Barbot, 2012). However, these models can only assume planar faults and they not account for anelastic deformation. Consequently, such models cannot address the complex fold-and-thrust belt structures and the long-term mountain building processes. Therefore, to improve our physical understanding of how mountain belts behave in terms of seismicity, we need an orogen-scale approach that takes into account the evolution of complex mountain belt architectures from the long-term tectonic history.

To overcome these modelling limitations we use a physics-based self-consistent seismo-thermo-mechanical (STM) modelling approach, which captures the dynamics of both long-term orogen-scale deformation and short-term seismic behaviour. We analyze results of a series of numerical models of continent–continent collision where different plate convergence rates are systematically tested to study its effects on seismicity style. We characterise this style by analysing the Gutenberg–Richter distribution and corresponding b value obtained from the synthetic catalogue of each numerical simulation. To understand these results we analyze the rheological feedback between plate convergence rate and the brittle strength of crustal rocks. Then, we verify our numerical hypothesis calculating similar quantities for natural examples of collisional orogens (i.e., Alps, Apennines, Zagros and Himalaya).

2. Methods

2.1. Seismo-thermo-mechanical modelling

The employed numerical STM code (van Dinther et al., 2013b) combines conservative finite differences on a fully staggered grid and marker-in-cell techniques (Gerya and Yuen, 2003). The momentum, mass and heat conservation equations are implicitly solved using a visco-elasto-plastic rheology (Gerya and Yuen, 2007) on the non-deforming Eulerian grid. The advection of physical properties including viscosity, plastic strain and temperature is performed with the displacement of Lagrangian markers. The momentum equations include the inertial term to stabilize high-coseismic slip rates at small time steps. The employed visco-elasto-plastic rheology is based on a constitutive relationship between deviatoric stresses and strain rates $\dot{\varepsilon_{ij}}$ applying linear elasticity and non-Newtonian viscosity (Gerya and Yuen, 2007)

$$\dot{\varepsilon_{ij}} = \frac{1}{2G}\frac{D\sigma'_{ij}}{Dt} + \frac{1}{2\eta}\sigma'_{ij} + \begin{cases} 0 & \text{for } \sigma'_{II} < \sigma_{yield} \\ \chi \frac{\partial \sigma'_{II}}{\partial \sigma'_{ij}} = \chi \frac{\partial \sigma'_{ij}}{2\sigma'_{II}} & \text{for } \sigma'_{II} = \sigma_{yield} \end{cases} \quad (1)$$

where G is shear modulus and η is effective viscosity. $D\sigma'_{ij}/Dt$ is the objective co-rotational time derivative solved using a time explicit scheme and $\sigma'_{II} = \sqrt{{\sigma'_{xx}}^2 + {\sigma'_{xz}}^2}$ is the square root of the second invariant of the deviatoric stress tensor, and χ is a plastic multiplier connecting plastic strain rates and stresses (Gerya and Yuen, 2007). Viscous creep is computed in terms of deformation invariants and depends on strain rate, temperature, and pressure (Ranalli, 1995). The viscous component of the deformation is then calculated as a combination of diffusion and dislocation creep. Plastic behaviour is taken into account assuming a non-associative Drucker–Prager yield criterion. Evaluated at each Lagrangian marker, plasticity sets in when the square root of the second invariant of the deviatoric stress tensor reaches the local pressure-dependent yield strength ($\sigma'_{II} = \sigma_{yield}$)

$$\sigma_{yield} = C + \mu_{eff}\ P, \quad (2)$$

where C is the cohesion. An important component in the yield criterion is the friction coefficient. Following the approach in van Dinther et al. (2013a), we apply a strongly rate-dependent friction formulation (e.g., Ampuero and Ben-Zion, 2008) in which the effective friction coefficient μ_{eff} depends on the visco-plastic slip velocity $V = (\sigma_{yield}/\eta_m)\Delta x$. Here η_m is the local viscosity, σ_{yield}/η_m is the square root of the second invariant of the visco-plastic strain rate ($\dot{\varepsilon}_{II}$) and Δx is the Eulerian grid size. This allows us to calculate the effective steady-state friction (μ_{eff}) coefficient at every marker as a function of slip rate V as

$$\mu_{eff} = \mu_s(1-\gamma) + \mu_s \frac{\gamma}{1+\frac{V}{V_c}} \quad (3)$$

$$\gamma = 1 - (\mu_d/\mu_s) \quad (4)$$

where μ_s and μ_d are static and dynamic friction coefficients, respectively. V_c is the characteristic velocity at which half of the friction change has occurred, and γ represents the amount of slip velocity-induced weakening if γ is positive, or strengthening if γ is negative. For all lithologies, the velocity weakening frictional formulation is parameterized using $\gamma = 0.7$ and $V_c = 4.4$ cm/yr, following van Dinther et al. (2013b). Full details of this method are provided in Gerya and Yuen (2007) and van Dinther et al. (2013b).

2.2. Model setup

The initial 2D model setup consists in a 4000 × 250 km computational domain (Fig. 1). Two 1700-km-long continental plates were separated by a 600-km-long oceanic plate. Both continental plates and an oceanic are composed of an upper crust, lower crust and lithospheric mantle. The visco-elasto-plastic thermomechanical parameters of these lithologies are based on a range of laboratory experiments (Table 1). The models use a grid resolution of 2041 × 401 nodes with variable grid spacing. This allow a minimum grid resolution of 400 m in the area subjected to largest deformation. More than 28 million Lagrangian markers carrying material properties were used in each experiment. The model has free slip boundary conditions and a permeable lower boundary with an infinity-like external free slip and external constant temperature conditions at 1670 km depth (Burg and Gerya, 2005). The free surface boundary condition atop the crust is implemented by using a "sticky air" layer (Schmeling et al., 2008) with low density (1 kg/m^3) and viscosity (10^{17} Pa s). The model is kinematically driven using internal boundary conditions located at 1000 and 3000 km (Fig. 1), which allow to impose an initial convergence rate of 10 cm yr^{-1}. The thermal structure of the oceanic lithosphere was calculated from the half space cooling model (Turcotte and Schubert, 2002) for a given plate age of 70 Myr (Fig. 1b). The initial continental geotherm was set using values of 0 °C at the surface and 1300 °C at 142 km depth. The thermal gradient used within the mantle was quasi-adiabatic (0.5 °C/km). Gravitational acceleration of 9.81 m s^{-2} was used in the model. To initiate subduction a weak zone was imposed on the right ocean–continent transition. The weak zone cuts through the whole lithospheric mantle with an angle of ∼30° and is characterised by weak plastic strength (1 MPa) and wet olivine rheological parameters (Ranalli, 1995).

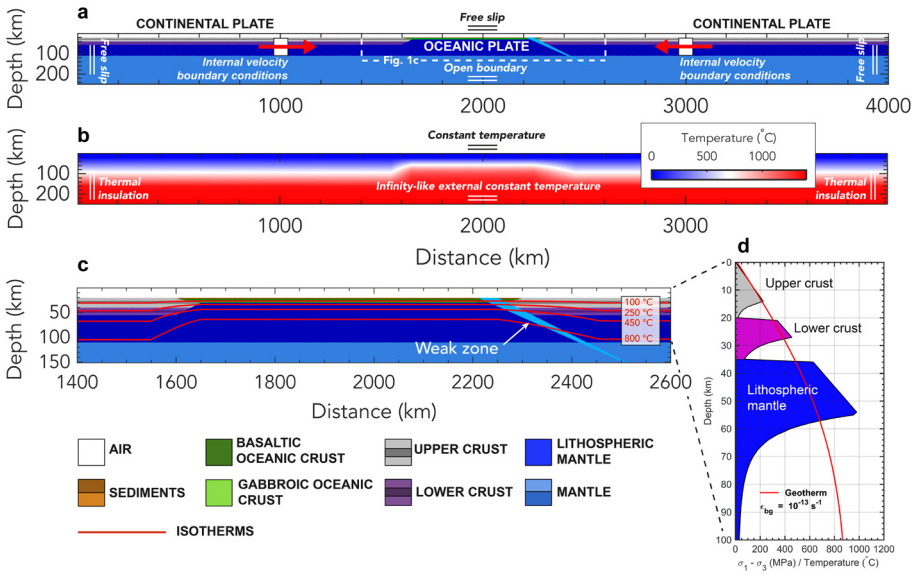

Fig. 1. 2D setup. (**a**) Initial composition map including boundary conditions. (**b**) Initial temperature distribution. (**c**) Zoom of oceanic plate with initial thermal structure in red. Plate convergence rate is applied at 1000 km for the left plate and 3000 km for the right plate. (**d**) 1D lithospheric strength profile and the corresponding initial geotherm. (For interpretation of the references to colour in this figure legend, the reader is referred to the web version of this article.)

Table 1
Rheological parameters. ρ_0 is the reference density, E_a is the activation energy, V_a is the activation volume, n is the stress exponent, η_0 is the reference viscosity, Hr is the radiogenic heat production, G is the shear modulus, μ_s is the static friction coefficient and λ is the pore-fluid pressure factor (P_{fluid}/P_{solid}). Other properties for all rock types: cohesion (C) is 1 MPa (Schultz, 1995), specific heat capacity (C_p) is 1000 J kg^{-1} K^{-1}, thermal conductivity (k) is in W m^{-1} K^{-1} at T_K and P_{MPa}, thermal expansion $\alpha_\rho = 3 \times 10^{-5}$ K^{-1} and compressibility $\beta_\rho = 1 \times 10^{-5}$ MPa^{-1}.

Material flow law[a]	ρ_0[b] (kg m^{-3})	E_a[a] (kJ mol^{-1})	V_a[a] (J/bar)	n[a]	η_0[a] (Pa^n s)	Hr[b,c] (μW m^{-3})	k[a] (W m^{-1} K^{-1})	G[d] (GPa)	μ_s[e,f]	λ
Sediments (Wet Qz)	2600	154	1.2	2.3	1.97×10^{17}	1.5	$[0.64 + 807/(T + 77)]$ $exp(4\ 10^{-5} P)$	25	0.35[g]	0
Upper cont. crust (Wet Qz)	2750	154	0.8	2.3	1.97×10^{17}	0.25	$[0.64 + 807/(T + 77)]$ $exp(4\ 10^{-5} P)$	25	0.6	0
Lower cont. crust (Mafic Granulite)	3000	445	0.8	4.2	1.25×10^{21}	1.5–4.0	$[0.64 + 807/(T + 77)]$ $exp(4\ 10^{-5} P)$	25	0.6	0
Upper oc. crust (Wet Qz)	3000	154	0.8	2.3	1.97×10^{17}	0.25	$[1.18 + 974/(T + 77)]$ $exp(4\ 10^{-5} P)$	25	0.5	0.95[h]
Lower oc. crust (Plg-An 75%)	3300	238	0.8	3.2	4.8×10^{22}	0.0022	$[1.18 + 974/(T + 77)]$ $exp(4\ 10^{-5} P)$	25	0.6	0
Mantle (Dry Olivine)	3300	532	0.8	3.5	3.98×10^{16}	0.0022	$[0.73 + 1293/(T + 77)]$ $exp(4\ 10^{-5} P)$	67	0.6	0

[a] Ranalli (1995); [b] Turcotte and Schubert (2002); [c] Rudnick and Fountain (1995); [d] van Dinther et al. (2013b); [e] Di Toro et al. (2011); [f] Del Gaudio et al. (2009); [g] Den Hartog et al. (2012); [h] Seno (2009).

2.3. Modelling procedure

The modelling approach comprises two steps: (1) long-term evolution, namely the closure of the oceanic basin, the subsequent continent–continent collision and mountain building, which is followed by (2) short-term seismic cycle, which simulate cycles of reoccurring interseismic and coseismic periods. Prior to the first modelling stage we define the initial geometry, rock properties, and temperature distributions (Fig. 1). Then we simulate the long-term evolution of a generic convergent margin, from subduction to collisional orogeny using a time step of 1000 yr. In this stage the inertia is negligible and friction is constant. Typical model evolution leads to self-sustaining subduction of the oceanic plate beneath the continental plate, followed later by continent–continent collision. In the second (short-term) modelling stage, the simulation starts with the distribution of physical properties (e.g., stress distribution, temperature, viscosity, and other material properties) from the long-term simulation. The time step is progressively decreases to 5 yr, while the inertia term and rate-dependent friction are activated (van Dinther et al., 2013b). Stress build up occurs as elastic strain is accumulated. Differential loading due to rheological discontinuities, tectonic asperities, temperature, and viscosity distribution causes stresses to be concentrated in different regions. In a typical seismic cycle, when the maximum strength is locally reached, the instability is fed through the feedback of decreasing viscosities. This increases slip velocities, which decreases the slip rate-dependent friction and strength, and in turn decreases viscosities even further. Spontaneous rupture propagation occurs because stresses are increased ahead of the rupture front to balance the dropping stresses within the rupture and to thereby maintain a static equilibrium. Finally, healing of strength occurs as slip velocities decrease.

2.4. Evaluating the Gutenberg–Richter distribution and b value

For each numerical experiment we analyze all rupture events to determine their downdip rupture width (W). These events occurring throughout the orogen are recognized using a Rupture Detector Algorithm (RDA), which analyzes each Lagrangian marker continuously. If its velocity exceeds a threshold of 9.0×10^{-9} m s^{-1},

while simultaneously stresses drop more than 0.4 MPa that marker's physical properties are stored in a synthetic data set. Subsequently markers are grouped into one event when they occur within 400 m of a marker that ruptured this or the previous time step. The rationale for choosing these thresholds comes from the minimally common stress drop (Allmann and Shearer, 2009) and our Eulerian grid size of 400 m, respectively. The sensitivity of these thresholds is tested and only introduces minimal variations in actual b values and number of events.

From these spontaneous rupture paths we measure the rupture width (W) to estimate the moment magnitude (M_W) using the empirical scaling relations in Wells and Coppersmith (1994). This empirical relationship is available from regression analysis based on a large numbers of events in nature:

$$M_W = a + b\,log\,(W), \tag{5}$$

where a and b are coefficients that vary with the style-of-faulting (i.e., normal or reverse faulting). We chose Wells and Coppersmith (1994) because they include various types of faulting and different tectonic environments. From these spontaneous synthetic events, we determine a single Gutenberg–Richter distribution for the entire orogen. The corresponding b values of these power law distributions are then estimated using the maximum curvature method (MAXC) (e.g., Marzocchi and Sandri, 2003). First, the completeness magnitude M_c is given by the probability density function of the magnitudes $M \geq M_c$

$$P(m) = b\,log(10)10^{b-(M-M_c)}. \tag{6}$$

Then, the b value is estimated with Aki's maximum likelihood method corrected for binned data (Tinti and Mulargia, 1987)

$$b = \frac{1}{log(10)\Delta m}\,log\left(1 + \frac{\Delta m}{\hat{u} - M_c}\right); \tag{7}$$

where $\hat{u}$ is the sampling average of the magnitudes and the event magnitudes are binned into magnitude bins of $\Delta m = 0.1$–0.3. We want to point out that we use this formula rather than the commonly used (e.g., Utsu, 1966) corrections because it gives more accurate and stable results under varying sample sizes (Marzocchi and Sandri, 2003). To estimate the error of the b value we use (Marzocchi and Sandri, 2003)

$$\sigma_b = 2.30\,\hat{b}\,\sqrt{\frac{\sum_{i=1}^{N}(M_i - \hat{u})^2}{N(N-1)}} \tag{8}$$

in which $\hat{b}$ is the b value that maximizes the likelihood function (Fisher, 1950), according to

$$\hat{b} = \frac{1}{log(10)(\hat{u} - M_{thresh})}, \tag{9}$$

where N is the number of earthquakes and M_{thresh} is the threshold magnitude, which corresponds to the minimum magnitude of completeness of the catalogue. These equations provide a reliable estimation in the presence of possible (time/spatial) variations of the b value (Marzocchi and Sandri, 2003).

3. Results

In this section, we outline the main results obtained from two sets of numerical experiments. The first set of numerical experiments (set A) were designed to cover systematically the same cumulated convergence (i.e., 1.8 km), assuming a range of convergence velocities from 10 to 50 mm yr^{-1}. A second set of numerical experiments (set B) is designed to study the importance of orogenic type and geometry on seismic behaviour with respect to the role of convergence rate. This is accomplished by increasing the radiogenic heat production of the lower crust of the upper plate, which changes the orogens geodynamic evolution and the resulting orogenic structure. For the reference model of each set of numerical experiment, we describe the general development of the post-subduction collisional orogeny from the long-term evolution; subsequently, a description of the short-term seismicity is given in order to characterise the seismicity style. Finally we quantify this seismicity using the Gutenberg–Richter distribution and the b value, which are used to evaluate the role that the plate convergence rate has in controlling the seismic behaviour of orogenic belts.

3.1. Set A: long-term mountain building

In all experiments, a fixed convergence rate of 10 cm yr^{-1} is imposed during the early phases of the models, which consist of oceanic plate consumption and ocean closure. As the incipient phase of continent–continent collision starts, the convergence rate gradually steps down to a lower value (from 10 cm yr^{-1} to a value in the range between 5 and 1 cm yr^{-1}). Therefore, each model exhibits the same behaviour during the subduction stage. The collisional regime has very similar features for models with different convergence rates (Fig. S1)—no significant differences in shape and size of the orogen and subduction dip-angle are observed.

The collisional regime with a convergence rate of 50 mm yr^{-1} is greatly affected by the buoyant and rheologically weak materials scraped off and accreted at the overriding plate margin. At the onset of collision, rocks of the crustal root affect the base of the plates' contact, increasing the degree of rheological coupling. As collision continues, more crustal material is accreted at the frontal margin, raising the topography and thus building up compressional stresses within the upper plate. The final structure of this collisional zone is characterised by an asymmetric fold-and-thrust belt structure, in which the stiff lithospheric edge of the right continental plate acts as a buttress, thus separating an orogenic wedge marked by different deformation styles (Fig. 2a). The pro-foreland basin and the orogenic wedge are dominated by simple shear deformation and nappe stacking. On the other side, the retro-foreland basin is characterised by pure shear shortening, thickening of the crust, back-thrusting and vertical exhumation of deep lithospheric mantle slices along the buttress. Approximately half of the 50 mm yr^{-1} convergence is absorbed by crustal shortening across the orogenic wedge (22 ± 4 mm yr^{-1}), while the remainder is accommodated through stable viscous shear along the deeper portion of the downgoing continent.

3.2. Set A: short-term seismicity

Results from the short-term seismicity shows a wide domain subjected to brittle-plastic faulting: beneath the pro-foreland basin, normal-faulting events propagating in the lower continental plate (Fig. 2b). Due to temperature-dependent mechanical properties of the lithosphere, such ruptures are mainly located in the brittle-plastic part of the upper/lower crust and sporadically nucleate in the lithospheric mantle, but never at temperatures greater than 500 °C. Seismogenic deformation in the orogenic wedge (Fig. 2c) is largely driven by elastic strain accumulation along the main thrust, which is characterised by partially or fully locked interseismic periods and rapid coseismic rebound. Seismic energy release in this region is dominated by the largest events occurring on the megathrust, which nucleate at different depths and propagate both down- and upward. Within the retro-foreland basin we observe pervasive reverse faulting, which propagates from the deep crust up to the subsurface (Fig. 2d). Fault propagation is assisted by inherited lithospheric structures near the orogenic

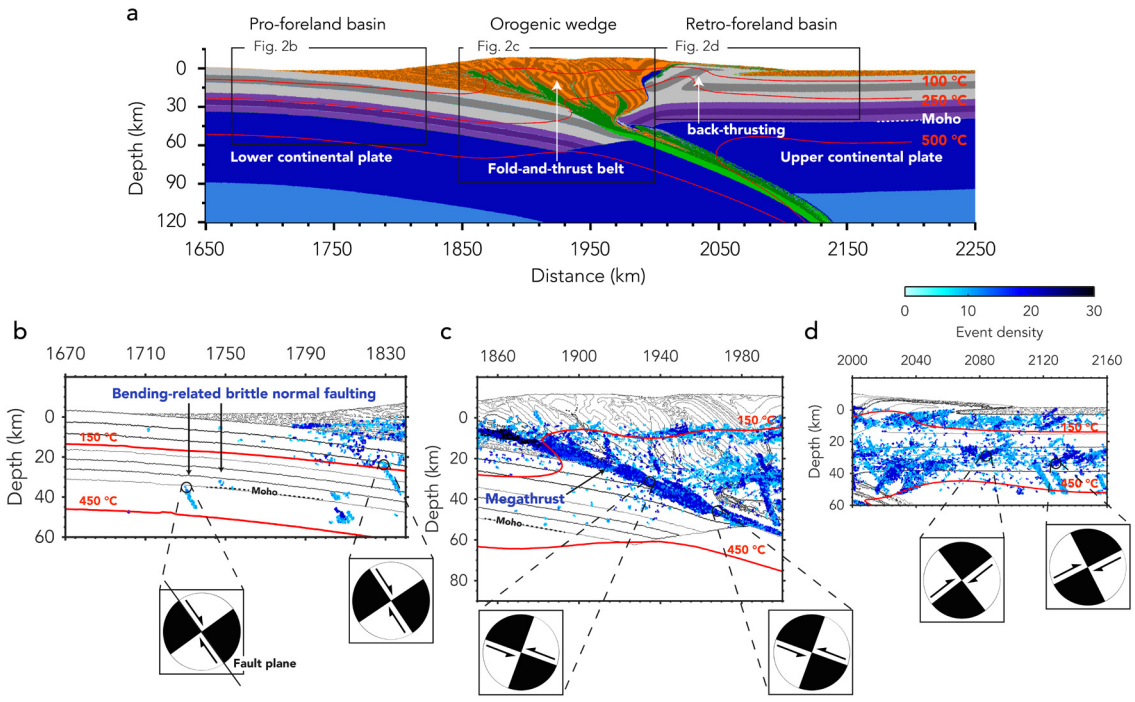

Fig. 2. Long-term (**a**) and short-term (**b–d**) characteristics of the Set A reference model for a plate convergence rate of 50 mm yr^{-1}. (**a**) Composition shows a broad orogen marked by nappe stacking in the pro-wedge and crustal shortening in the retro-wedge. The short-term spatial evolution of all rupture events within the (**b**) pro-wedge, (**c**) orogenic wedge, and (**d**) retro-wedge. The inferred focal mechanisms show a broad pattern of different style of faulting, which are consistent with the local tectonic regime.

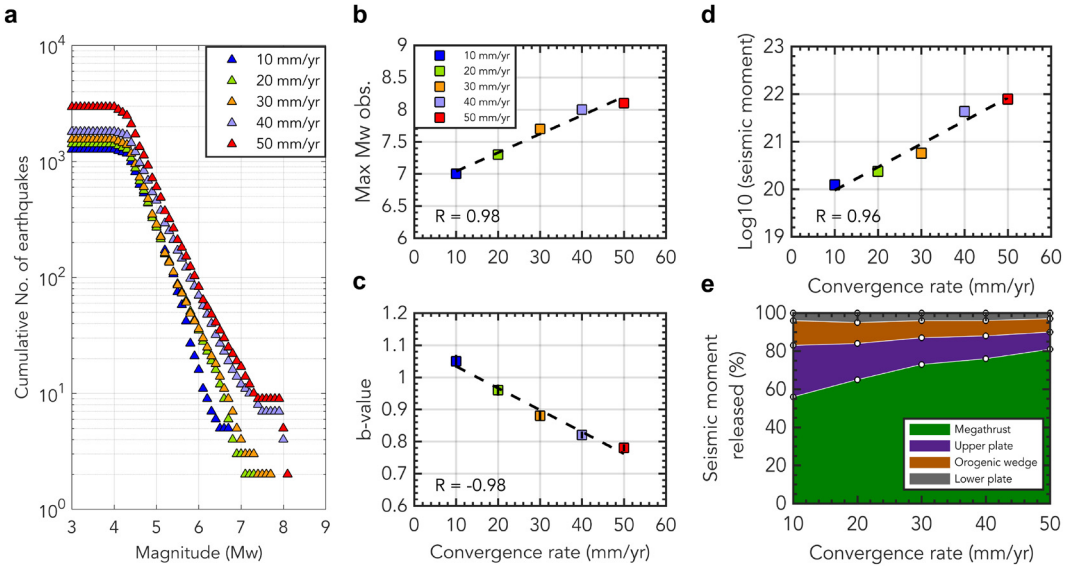

Fig. 3. Seismic behaviour of the reference models assuming the same amount of convergence (i.e., 1.8 km) and with plate convergence rate varying from 10 to 50 mm yr^{-1}. (**a**) Gutenberg–Richter distribution. (**b**) Relationship between plate convergence rate and estimated maximum magnitude. (**c**) Relationship between plate convergence rate and *b* value. (**d**) Relationship between plate convergence rate and cumulative seismic moment released. (**e**) Seismic moment released (in percentage) between the megathrust, upper plate, orogenic wedge and lower plate, as a function of plate convergence rate. Dashed lines indicate the regression line.

wedge, which promote localized deformation and coseismic faulting up to the subsurface. Beneath the retro-foreland basin, brittle faulting occurs on young faults that are marked by coseismic events.

3.3. Set A: Gutenberg–Richter parameters

The rupture width of these events is scaled according to empirical scaling relations (Wells and Coppersmith, 1994, Section 2.4) to plot the corresponding moment magnitude versus the number of events larger than each size (Fig. 3a). The resulting frequency–magnitude distribution follows a power-law, as earthquakes do in nature (e.g., Pasquale et al., 2010). Most seismic cycle models, including our previous subduction zone models (van Dinther et al., 2014), do not capture this important statistical feature of earthquake occurrence. Due to the occurrence of events on many smaller faults, throughout the orogen and the megathrust interface, these models do produce a Gutenberg–Richter distribution. We quantify the behaviour of seismicity through analyzing the parameters describing this Gutenberg–Richter distribution.

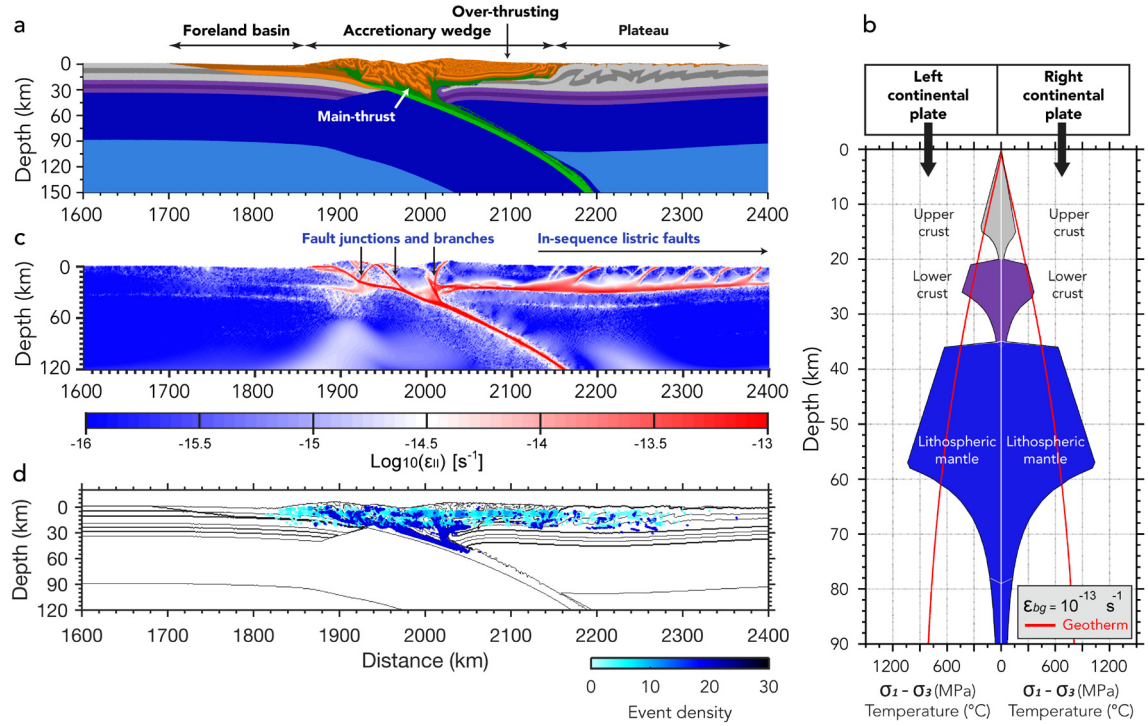

Fig. 4. Set B numerical experiments simulating a warmer and broader orogenic belt (plate convergence rate: 50 mm yr^{-1}). A higher radiogenic heat was applied in the upper continental plate with respect to the reference model (see Table 1). (**a**) Compositional map showing the orogenic wedge development, backthrusting and crustal shortening, overthrusting of the orogenic wedge, and broadening of the continental plateau. (**b**) 1D strength envelope profile of the left and right continental plates. (**c**) Strain rate map. Fault activation due to continent–continent collision occurs mainly at the main thrust, in the orogenic wedge, and in the upper plate. (**d**) Rupture event density map. Seismogenic faulting is in agreement with the strain rate field.

Comparing models with different convergence rates (varying from 10 to 50 mm yr^{-1}) but the same amount of convergence, we observe the following relationship: (*i*) the cumulative number of events increases for higher convergence rates (Fig. 3a) and (*ii*) $M_{W\,max}$ indicate a positive and linear correlation with plate convergence rate (from 7.0 to 8.1, Fig. 3b). Following the same line of reasoning, we compared *b* values and convergence rate and found a linear and negative correlation between these parameters (from 1.05 to 0.78, Fig. 3c). Moreover, the cumulative seismic moment released shows a linear and positive relations with plate convergence rate (Fig. 3d). The Pearson linear correlation coefficient (R) demonstrates a good linear fit between plate convergence rate and $M_{W\,max}$ ($R = 0.98$, Fig. 3b), *b* value ($R = -0.98$, Fig. 3c) and seismic moment released ($R = 0.96$, Fig. 3d). To evaluate the significance of these correlations we extracted the *p* value, which represents the significance level to reject the null hypothesis that these correlations occur randomly irrespective of convergence rate. The result of this analysis indicates that the correlations are highly significant between convergence rate and $M_{W\,max}$ (p value $= 0.013$) and *b* value (p value $= 0.003$), meaning that they are significant at 97.7% (Fig. 3b, c) and 95.7% (Fig. 3d), respectively. To further understand where the seismic energy is released in different regions, we divided the domain in (1) megathrust, (2) upper plate, (3) orogenic wedge and (4) lower plate. Subsequently, we compare their distributions with respect to the convergence rate (Fig. 3e). We observe a dominant role of the megathrust, which releases 81% of seismic moment for convergence rates of 50 mm yr^{-1}. This progressively decreases down to 56% when for convergence rate of 10 mm yr^{-1}. On the other hand, a decrease in the seismic moment released in the megathrust results in an increase in other regions, namely for the orogenic wedge and the upper plate, whereas the lower plate value remains almost constant. Overall, increasing convergence rate thus transfers seismic energy release from the megathrust into neighbouring regions.

3.4. Set B: role of mountain ranges architecture

The geometry of tectonic structures is typically considered to be of first order importance in the control of seismic behaviour of orogenic mountain belts (e.g., Avouac, 2015; Bollinger et al., 2004; Cheloni et al., 2014; Chen et al., 2016). To compare that importance with respect to the role of plate convergence rate we performed a second set of numerical experiments with a distinctly different orogenic architecture. In the models of set B the lower crust of the upper plate has higher concentration of radiogenic elements of 4 μW/m^3 (Table 1) with respect to the previous set A, as observed in the Sikkim Himalaya (Rudnick and Fountain, 1995).

The early stages of the long-term development of the orogen are very similar to the previous set of models (Fig. 4). Sediments are accreted in the orogenic prism and the lithospheric edge acts as a buttress, while the upper plate is only slightly ablated due to shearing between the two plates. At the onset of continental collision, however, the warm upper plate edge is warped up due to the push from the material of the accretionary prism. The present model hence, shows, yielding and crosscutting of the upper plate due to thermal softening at the indentation zone and in the retro-foreland basin. As collision continues, crustal stacking produces the progressive rightward migration of the suture zone and the development of an elevated plateau. The final structure of this coupled collisional zone is characterised by a thick and hot crustal wedge overlying a subducting plate with a broad asymmetrical collisional zone (Fig. 4a). Also notable is the different deformation styles that characterised the retro-wedge (Fig. 4b): beneath the orogenic wedge the crustal detachment is dominated by simple shear, whereas far from wedge (in the retro-foreland basin) the plateau is characterised by pure shear thickening. The wide collisional zone thus leads to an asymmetric one-sided structure. As a result, stresses are mainly compressive with minor extension due to plate bending. Also notable is the difference in the ther-

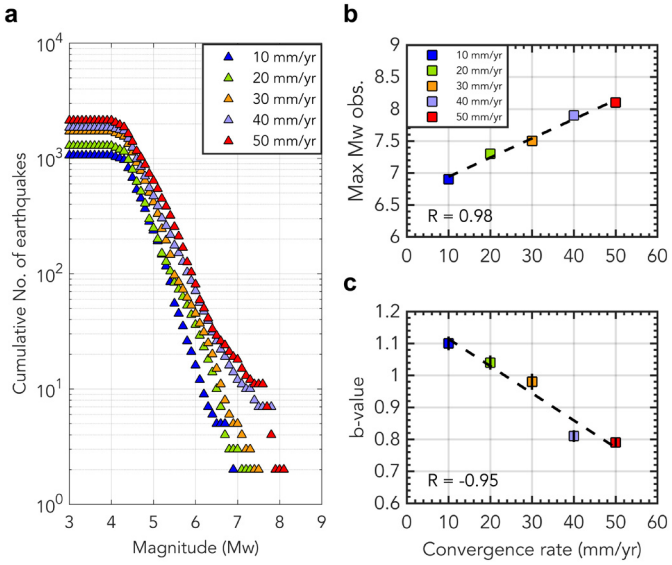

Fig. 5. Results from the model shown in Fig. 4 (set of experiments B) assuming the same amount of convergence (i.e., 1.8 km): Gutenberg–Richter distributions and dependence of b and maximum M_W observed on plate convergence rate. (**a**) Frequency–magnitude distribution for the five simulations. (**b**) Relationship between plate convergence rate and maximum magnitude estimated. (**c**) Relationship between plate convergence rate and b value estimated. Dashed line indicates the regression line.

mal evolution of the pro- and retrowedge. This nicely underscores the significance of radiogenic material in controlling the rheological conditions that are attained by any given block of the crust.

These different deformation styles lead to a distinctly different spatial distribution of seismicity (Fig. 4c). The large collision zone results in a compressional domain in the frontal part of the orogenic wedge with some extensional areas due to the plate bending beneath the foreland basin, which are characterised by normal-faulting events. The megathrust geometry along the inherited subduction channel is comparable to the previous set of experiments, although it branches into several fault segments due to crustal softening in the upper plate. Because of the yielding of the warm upper plate, the orogenic wedge overthrusts the retro-foreland domain causing a sequence of back-thrusts far from the orogenic wedge (in the plateau). These results illustrate that thermal crustal properties affect the structure and geometry of collisional orogens and thereby their spatial distribution of seismicity.

The characterisation of this distinctly different orogenic structure seismicity, through the Gutenberg–Richter distribution is, however, surprisingly similar with respect to the previous set of numerical simulations (Fig. 5). Comparing these models with the previous set A of numerical experiments, we observe that the positive relations between plate convergence rate and the cumulative number of events (Fig. 5a) and the maximum magnitude $M_{W\,max}$ (from 6.9 to 8.1, Fig. 5b) are confirmed. Moreover, the resulting b values show a linear and negative trend for higher convergence rates, with values from 1.10 to 0.79 (Fig. 5c). Although the absolute values of $M_{W\,max}$ and b are slightly different compared to the previous set A (Fig. 3), the correlation coefficient confirms the linear relations between both of them and plate convergence rate.

These results therefore indicate that small variations in the radiogenic content of crustal rocks may have obvious effects on both the long-term formation of a collisional orogen and the short-term seismicity. Radiogenic heating increases the temperature of crustal rocks, producing a high and broad plateau and thus affecting the spatial distribution of seismicity. Despite the fact that this hot tectonic environment influences the location of seismogenic faults, we stress that the characterisation of the seismic behaviour through the Gutenberg–Richter statistics is determined by the convergence rate acting in the subduction/collision system rather than by geometry of the orogen itself.

4. Discussion

These results shed light on the correlation between plate convergence rate and seismicity characteristics at continent–continent collisional margins and lead to several interesting implications. We first discuss the physical mechanisms responsible for the control of plate convergence rate on the seismic behaviour of orogenic belts. Subsequently, we make a comparison between the Alps, Apennines, Zagros and Himalaya and our numerical experiments. Finally, we discuss involved uncertainties and modelling limitations.

4.1. How does convergence rate control seismicity?

The seismic behaviour of mountain belts is determined by the location of elastic strain build up within strong elastic–brittle layers (Scholz, 2002), while weaker layers are presumed to creep and deform aseismically (e.g., Doglioni et al., 2011; Pasquale et al., 2010). The strength of the Earth's lithosphere depends on several rheological properties such as stress, strain rate, strain history, composition, and most importantly temperature (e.g., Chen and Yang, 2004; Maggi et al., 2000). In our numerical experiments, as well as in nature, both the large-scale temperature field and the strain rate distribution are mainly controlled by the plate convergence rate. The subsequent control of temperature and background strain rate on the strength and rheology of the lithosphere can be visualized in a simplified manner using 1D lithospheric strength profiles (Fig. 6). These profiles are based on same lithological stratification of continental lithosphere and the same rheological properties as in the 2D simulations. To compose these, we used the Moho temperatures (T_{Moho}) reflecting the reference temperature of the lithosphere and a background strain rate ($\dot{\varepsilon}_{bg}$) as reference parameters. An increase in convergence rate, for instance, allows for deeper subduction of lower temperatures, thereby deepening the brittle extent of the crust (Fig. 6a). Thus, the brittle behaviour of the upper crust deepens, and the lower crust becomes more brittle. Similar behaviour can be found for the feedback through strain rate, because higher convergence rates lead to larger background strain rates, thereby extending the brittle failure depth (Fig. 6b and Fig. S4). Consequently, the lower crust is to a larger extent seismogenic. To quantify in which form plastic strain is released throughout the orogen, we further analyzed the partitioning between seismic and aseismic deformation. Results show that within the seismogenic depth range, seismic/aseismic strain vary with plate convergence rate (Fig. 6c). For a range of convergence rate varying from 10 to 50 mm yr^{-1}, seismic strain increases (from 19% to 58%) when the rate of collision between the two continental plates rises. Also, seismicity is observed to migrate from the megathrust into the orogenic wedge as convergence rate decreases. This more distributed form of brittle deformation is also accompanied by a larger contribution of ductile deformation, thereby reducing the magnitude of the largest events. These results thus demonstrate that the competition between seismic and aseismic strain has a strong influence on the seismic behaviour of mountain belts. Seismicity tends to localize on the megathrust when convergence rate increases, while a more distributed seismicity yields to seismic events of smaller sizes for slower convergent margins. This rheological feedback has important implications for the seismogenic response of the system. On the megathrust, temperatures (and stresses) increase with depth, whereas viscosities decrease beyond 60–70 km depth, reaching near upper mantle values at ∼80–90 km depth. Consequently, thermally and stress driven creep governs a spontaneous, conditionally stable downdip

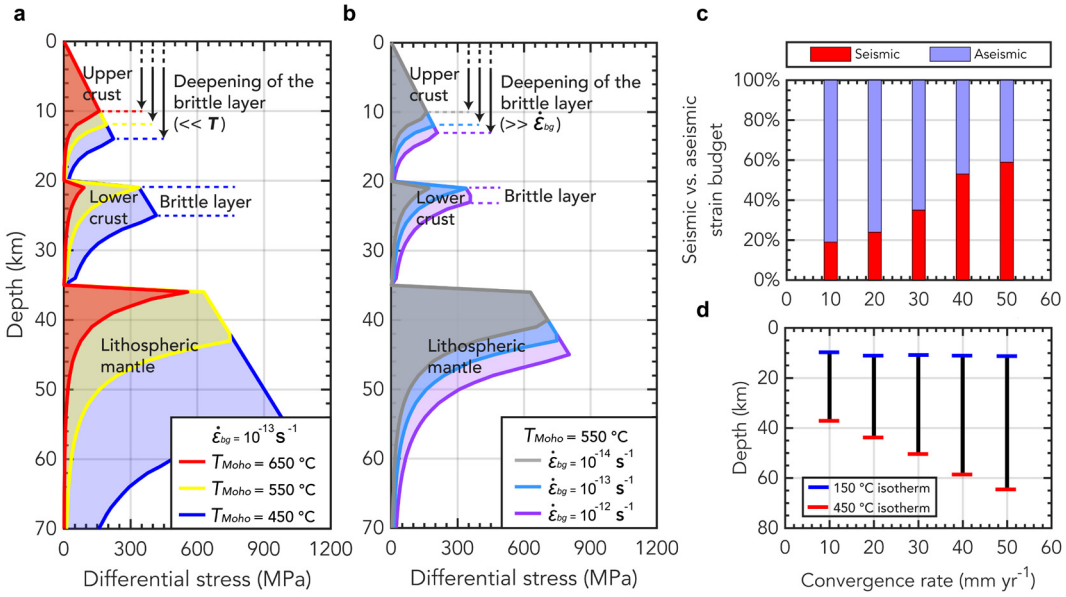

Fig. 6. 1D lithospheric strength profiles taken from the initial lithological sequence of the continental plate show the representative distribution of differential stress with depth, as a function of (**a**) temperature and (**b**) strain rate, which are both controlled by plate convergence rate. Note that the temperature distribution, and strain rate field, characterise the deepening of brittle behaviour within the upper crust and the brittle–ductile transition of the lower crust with increasing convergence rate. (**c**) Quantitative view of the relationship between seismic/aseismic strain and plate convergence rate throughout the orogen. Panel (**d**) shows the deepening of the megathrust seismogenic zone for higher convergence rates. The seismogenic downdip width is confined by the 150°C isotherm (where friction switches from velocity-strengthening to velocity-weakening) and the 450 °C isotherm (thermally driven brittle–ductile transition).

transition zone between temperatures of 350–450 °C. Ruptures initiate above it, propagate within it, and arrest below it as ductile shearing relaxes stresses. Results in Fig. 6d indicate that the location at depth of such brittle/ductile transition zone depends on the convergence rate. As a result, the rupture width (and the corresponding maximum magnitude $M_{W\,max}$) changes according to this rheological feedback.

We next investigated the possible correlation between the increasing of convergence rate and the deepening of the brittle strength. To do so, we analyze the depth distribution of all rupture events of each model performed during the first set of experiment. These synthetic hypocentre distributions show that earthquakes nucleate over a larger depth extent when convergence rates are higher (Fig. 7a). The depth distribution gradually changes with increasing of plate convergence rate, from unimodal (i.e., upper crust confined) distributions for low convergence rates (10–30 mm yr^{-1}) to bimodal (i.e., upper and lower crust seismogenic) distributions for high convergence rates (40–50 mm yr^{-1}, Fig. 7a). The bimodal depth distribution of hypocentres for rapidly converging orogens thus confirms the predictions from the simplified continental 1D strength profiles. Slowly converging orogens (i.e., with higher temperature and lower background strain rate) have a largely ductile lower crust, while rapidly converging orogens (i.e., with lower temperature and higher background strain rate) have a second brittle layer within the lower crust.

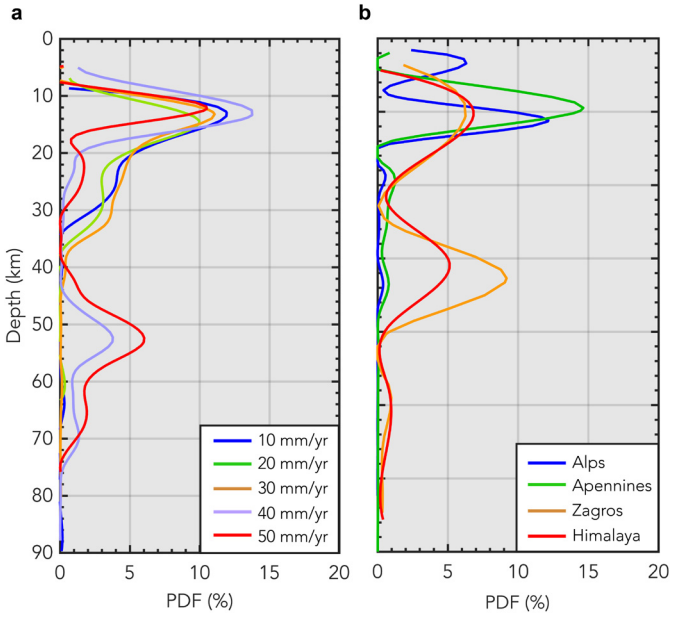

Fig. 7. Probability density distribution of hypocentres versus depth for (**a**) numerical experiments and (**b**) nature cases ($M_W > 2.5$). Modelling results in (**a**) indicate a unimodal, upper crust confined, distribution of earthquakes in the case of lower converging rates (10, 20, and 30 mm/yr). Highly converging mountain belts show instead a bimodal distributions of earthquakes, since both the upper and lower crust are seismogenic. These results find agreement with the seismicity data from the four continent–continent mountain belts analyzed.

4.2. Comparison to natural examples

4.2.1. Relation between plate convergence rate and depth distribution of seismicity

To verify this physical mechanism we analyze whether earthquake data also show the conversion from a ductile lower crust to a more brittle one for rapidly converging orogens. Using the U.S. National Earthquake Information Center (NEIC) catalogue, we collected the distribution earthquakes with magnitude ≥4.5 occurring at depths from 0 to 70 km within four representative continent–continent orogenic regions differing in plate convergence rate: Alps (2.3 ± 0.5 mm/yr), Apennines (5 ± 1 mm yr^{-1}), Zagros (25 ± 3 mm/yr), and Himalaya (38 ± 2 mm/yr). Latitude and longitude coordinates used to extract the earthquake data sets are listed in Table 2. As a result of the declustering procedure, the events that are closely related to each other spatially or temporally, and could be considered as aftershocks, are removed using the algorithm of Gardner and Knopoff (1974) included in the interactive software tool ZMAP (Wiemer, 2001). These natural data show a systematic difference in hypocentre locations between the

Table 2
List of latitude and longitude coordinates used to extract the earthquake data sets from the U.S. National Earthquake Information Center (NEIC) catalogue.

Mountain belt	Latitude	Longitude
Alps	45.322; 47.968	10.074; 13.271
	45.422; 47.754	8.074; 10.074
	43.053; 47.339	4.966; 8.053
Apennines	43.914; 42.120	8.35; 12.766
	42.375; 43.914	10.283; 14.183
	40.955; 43.914	11.821; 16.403
	39.952; 40.955	14.326; 17.238
Zagros	34.742; 37.632	43.198; 48.713
	31.504; 34.742	45.132; 52.998
	29.056; 31.504	49.307; 55.107
	26.51; 29.056	50.977; 57.437
Himalaya	25.945; 36.334	76.203; 83.321
	25.683; 36.334	83.321; 95.318

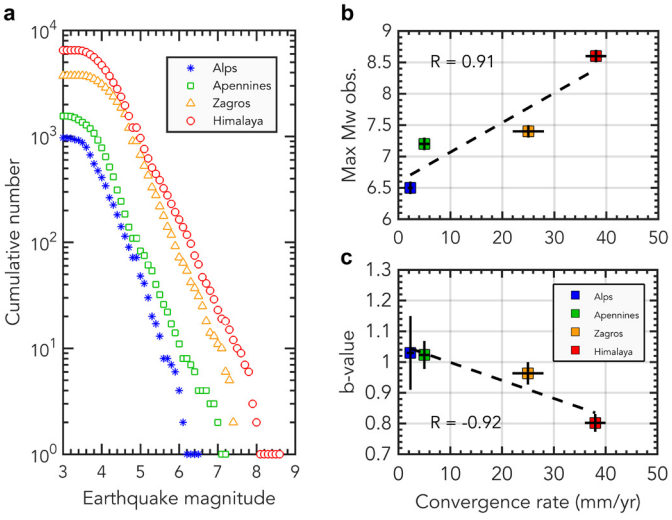

Fig. 8. (**a**) Frequency–magnitude distribution of earthquakes for events in the four orogenic belts considered. (**b**) Relationship between plate convergence rate and maximum magnitude observed in the NEIC catalogue. (**c**) Relationship between plate convergence rate and *b* value (see Methods). Dashed line indicates the regression line.

Alpine and Apennine chains and the Zagros–Himalayan environments (Fig. 7b). The slowly converging Alpine–Apennine orogenic systems are dominated by an upper crust confined, unimodal distribution of earthquakes. The rapidly converging Zagros and Himalayan regions, however, also reveal many earthquakes nucleating within the lower crust. This change from unimodal to bimodal hypocentre distributions was independently suggested by our models (Fig. 7a). These natural data thus support our mechanical explanation that the seismogenic domain is extended as the lithosphere is colder and background strain rate is higher with increasing converging velocities.

4.2.2. Relation between plate convergence rate and earthquake-size distribution

The same data sets are then used to analyze the relation between convergence rate and the Gutenberg–Richter parameters for each continent–continent collisional orogen studied (Fig. 8). To do so, earthquakes listed in the form of body wave (m_b) or local (M_L) magnitude are converted to moment magnitude (M_W) using the empirical global relations provided in Hanks and Kanamori (1979) and Scordilis (2006). The four different continent–continent orogens reveal a distinctly different frequency–magnitude distribution in accordance with their known seismicity patterns (Fig. 8a).

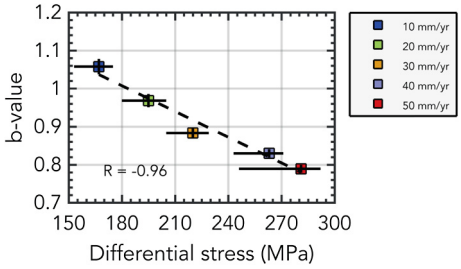

Fig. 9. *b* values versus average differential stress from the suite of reference simulations with different convergence rate (from 10 to 50 mm yr^{-1}). The differential stress is averaged over the whole orogenic belt domain over all interseismic periods. Black lines denote the range of *b* value error and the standard deviation of the differential stress, respectively. Dashed line indicates the regression line.

When we plot two of its governing Gutenberg–Richter parameters against each convergence rate from literature (Wang et al., 2001; Grenerczy et al., 2005; Tatar et al., 2002), we once again find a positive linear relationship with sufficient confidence ($R = 0.91$ in Fig. 8b and $R = -0.92$ in Fig. 8c, respectively). Therefore, these seismicity data support the hypothesis that an increasing in plate convergence rate leads to larger maximum moment magnitudes and smaller *b* values.

4.3. On the differential stress dependence of the b value

Several studies have suggested a relation between differential stress ($\Delta\sigma$) and the relative size distribution of earthquakes quantified by the *b* value. In the laboratory, acoustic emissions (AEs) from seismically active micro-cracks follow a power law analogous to the Gutenberg–Richter relation with decreasing *b* value for increasing $\Delta\sigma$ (e.g., Amitrano, 2003). More recently, other studies suggested this inverse and linear relation holds for tectonic earthquakes in continental areas (Spada et al., 2013; Scholz, 2015).

In our numerical experiments, the *b* value is also observed to decrease linearly as a function of the average differential stress (Fig. 9). This can likely result from the linear relation between stress and strain in the elastic constitutive equation (first part of eq. (1)). Moreover, Scholz (2015) demonstrated that the dependences of *b* value on confining pressure (Amitrano, 2003), mechanical strength of the crust (Pasquale et al., 2010) and focal mechanism (Schorlemmer et al., 2005; Doglioni et al., 2015) are in fact the result of the underlying differential stress. We propose that the convergence rate is in fact the ultimate first-order physical parameter governing the other physical parameters and thus the seismicity behaviour in mountain belts.

4.4. Limitations and uncertainties

4.4.1. Modelling limitations

The numerical model has the same limitations as the one previously applied to subduction zones (van Dinther et al., 2013b). In nature, earthquake ruptures occur within a three-dimensional, geometrically complex fault system with various scales of downdip and along-strike variations in its seismogenic behaviour. The lateral, third dimension is absent in our numerical model. That means that our two-dimensional plane strain model ignores lateral variations in interseismic stress buildup and rupture propagation. Compared to nature our model produces unrealistically long seismic events because of the large time step (i.e., 5 yr). This means that a simulated event or earthquake refers to the occurrence of rapid threshold-exceeding slip during which permanent displacement and stress drop occur along a localized interface. On the other hand, the presented results generally demonstrate a satisfactory agreement with a wide range of long- and short-term natural observations. Events in our numerical model have reasonable

downdip widths (which are used to estimate the moment magnitude), and similar behaviour to events in the laboratory model (van Dinther et al., 2013a). However, is important to stress that the small-scale complexities of each natural system are difficult to reproduce in a self-consistent lithospheric-scale model. Moreover, even excluding expected along-strike variations of the orogen, details of individual orogens cannot be expected to be reproduced in general models such as the ones of this study. In spite of these potential pitfalls, however, the number of salient but enigmatic observed features of the real collision zones that our models do succeed in reproducing is highly encouraging and provides useful insights.

4.4.2. Consistency of results using the NEIC catalogue

The usage of the USGS National Earthquake Information Center (NEIC) catalogue for the period 1905–2016 also requires a note of caution. The NEIC catalogue is a composite catalogue, whose heterogeneity could affect the estimation of b values (e.g., Kamer and Hiemer, 2015). We ultimately selected—for each continent–continent collision zone—the whole study region, rather than splitting those regions into segments of different volumes. We made this arbitrary choice because for comparison with the results obtained from our numerical experiments. Despite the presence of several mountain belts worldwide (e.g., Pyrenees and Dinarides), we chose these four study regions (i.e., Alps, Apennines, Zagros and Himalaya) because (1) differ in the tectonic structure, (2) are tectonically active, (3) show different seismic behaviour and (4) have a wide and representative spectrum of convergence rates. To investigate the influence of sample size, we repeated the analysis using some study regions cut in half. The resulting b values were not strongly affected ($\Delta b \leq 0.04$), although the relative error increases due to lower sample size. Since hypocentre depth is particularly difficult to estimate in these data sets, we integrated the analysis of local studies (e.g., Maggi et al., 2000; Jackson, 2002; Pasquale et al., 2010; Bragato and Slejko, 2005). This qualitative comparison shows that despite the uncertainties, our analysis remain sufficiently representative.

4.5. Seismic hazard implications

Despite inevitable modelling limitations and uncertainties from spatiotemporally limited data, the combination of the presented Gutenberg–Richter distribution results from numerical models and earthquake data in addition to a rheological analysis of the brittle strength supports the hypothesis that the seismicity in orogenic belts is fundamentally controlled by plate convergence rate. In profile view the tectonic structure of the orogen itself plays an important role for the spatial distribution of seismicity, although subordinate in terms of Gutenberg–Richter statistics. Plate convergence rate seems to control the forces driving seismic and aseismic deformation within these mountain belts. Low convergence rate in the Alps and Apennines is accommodated by moderate earthquakes and more ductile deformation, whereas a pervasive set of large earthquakes marks both the rapidly converging Zagros and Himalayan regions.

Probabilistic seismic hazard and risk assessment is determined by the ratio of large over small earthquakes (b value), $M_{W\,max}$, and the seismicity rate (a value) (e.g., Wiemer et al., 2009). Our results indicate that the seismicity rate is not the only hazard parameter affected by convergence rate. $M_{W\,max}$ and the relative amount of large earthquakes (i.e., lower b value) increase as well with increased convergence rate due to a wider seismogenic zone resulting from the feedback of temperature and background strain rate on brittle strength. This result does not agree with previous studies that do not account for this feedback, such as in theoretical studies (e.g., Molnar, 1979) and more simple analog and numerical models of subduction zones (Corbi et al., 2017). Moreover, global studies of earthquakes in subduction zones that do show large variability of b value, do not unequivocally support a correlation between convergence rate and b value (Nishikawa and Ide, 2014, $R = 0.22$) and $M_{W\,max}$ (Marzocchi et al., 2016). Although in similar studies a weak correlation between convergence rate and $M_{W\,max}$ has been proposed (Heuret et al., 2011, $R = 0.42$). The absence of a robust correlation in observations of subduction zones over the last decades could be explained by a too limited observational time period (McCaffrey, 2008) or ambiguity introduced by other parameters influencing megathrust seismicity at the same time. However, taking into account longer time series and rheological feedback, we suggest that the seismic hazard in rapidly converging regions is increased even further than expected when only taking seismicity rate and corresponding increased likelihood into account. Considering that the same line of reasoning is expected to hold for subduction zones, we would also expect seismic hazard, or at least $M_{W\,max}$, to increase with increasing subduction velocity.

5. Conclusions

We systematically studied the influence of convergence rate on seismicity in active continent–continent collisional orogens through using numerical models and a comparison with earthquake data. The most important results can be summarized as follows:

1. Cycles of spontaneous earthquake-like ruptures on non-a-priori-defined faults are for the first time simulated in a generic continent–continent collision zone. Using the developed, innovative seismo-thermo-mechanical approach, we simulate the feedback between long-term continental orogeny and relating deformation and short-term seismicity. Our results show physically consistent emergence of complex rupture events, both on- and off-megathrust. These events lead to a Gutenberg–Richter frequency–magnitude distribution, a key observational feature of seismicity, which is typically not reproduced in seismic cycle models.
2. These Gutenberg–Richter distributions suggest an inverse, linear relationship between plate convergence rate and b value. Also, these results indicate a positive, linear relationship between $M_{W\,max}$ and plate convergence rate. This means that plate convergence rate controls the seismic behaviour of mountain belts, both in terms of frequency and size of earthquakes. Collisional orogens with high convergence rates are manifested by pervasive seismicity, high magnitude of earthquakes and relative low b values. In contrast, decreasing convergence rates lead to relatively larger amounts of smaller earthquakes (i.e., increasing b value) and lower maximum magnitudes. Moreover, seismicity is observed to migrate from the main thrust into the orogenic wedge as convergence rate decreases. This more distributed form of brittle deformation is also accompanied by a larger contribution of ductile deformation, thereby additionally reducing seismic hazard for slower convergent margins.
3. High convergence rates reduce the average temperature of the orogen, thereby increasing the brittle portion of the crust at the expense of the ductile portion. Higher convergence rates, moreover, lead to larger background strain rates, which extend the brittle failure depth even further. This rheological feedback mechanism therefore suggests that for high collision rates the brittle strength is larger and, in turn, increases the capacity of seismogenic faults to store and release elastic strain energy.

4. Our analysis shows that the b value decreases linearly with differential stress for orogens with higher convergence rate, which agrees with laboratory experiments and natural data. Since differential stress in turn depends on the plate convergence rate, it supports our hypothesis that the convergence rate is in fact the ultimate first-order physical parameter governing the other physical parameters and thus the seismic behaviour of mountain belts.
5. These modelling results found a good agreement with general observations of seismicity patterns within the collisional orogens. Himalayan and Zagros orogens are mainly characterised by bimodal (i.e., upper and lower crust) distribution of earthquakes and a localized seismicity along the megathrust. The Alps and Apennines show instead an unimodal (i.e., upper crust confined) distribution of earthquakes and a more widespread, and less intense, seismicity.
6. Warm collision zones are manifested by the development of a high and broad plateau overlying a thick crustal wedge formed by continuous accretion of crustal slices. Results show that the location of seismogenic faults may change according to the regional stresses and the main tectonic structures. However, the resulting seismic behaviour is dominated by plate convergence rate.

First-order agreement between our models and data support the implications of our results and contributes to fill the gap left in modelling seismicity of collisional margins. Even though second-order effects can come from the tectonic structure of the belt itself, our findings suggests that convergence rate is a critical parameter for the seismic behaviour of mountain belts. Therefore, hazard studies should pay attention to this critical parameter as it, besides seismicity rate, also affects $M_{W\,max}$, b value, and is directly related to the distribution of stresses in the Earth's crust.

Acknowledgements

This study was funded by the SNF project Swiss-AlpArray SINERGIA. We thank E. Kissling, S. Wiemer and Y. Kamer for encouragement and for providing helpful background information. For constructive comments and discussions we thank G. Hetényi, J. Singer, S. Simuté and the STM-group. Numerical simulations were performed on ETH cluster Euler. We thank David Whipp and an anonymous reviewer for their constructive comments, which helped improve the paper considerably.

Appendix A. Supplementary material

Supplementary material related to this article can be found online at https://doi.org/10.1016/j.epsl.2017.10.053.

References

Allmann, Bettina P., Shearer, Peter M., 2009. Global variations of stress drop for moderate to large earthquakes. J. Geophys. Res., Solid Earth 114 (B1).
Amitrano, David, 2003. Brittle–ductile transition and associated seismicity: experimental and numerical studies and relationship with the b value. J. Geophys. Res., Solid Earth 108 (B1).
Ampuero, J-P., Ben-Zion, Y., 2008. Cracks, pulses and macroscopic asymmetry of dynamic rupture on a bimaterial interface with velocity-weakening friction. Geophys. J. Int. 173 (2), 674–692.
Avouac, J.P., 2015. Mountain building: from earthquakes to geologic deformation. Treatise Geophys. 6, 381–432.
Bollinger, L., Avouac, J.P., Cattin, R., Pandey, M.R., 2004. Stress buildup in the Himalaya. J. Geophys. Res., Solid Earth 109 (B11).
Bragato, P.L., Slejko, D., 2005. Empirical ground-motion attenuation relations for the eastern Alps in the magnitude range 2.5–6.3. Bull. Seismol. Soc. Am. 95 (1), 252–276.
Burg, J-P., Gerya, T.V., 2005. The role of viscous heating in Barrovian metamorphism of collisional orogens: thermomechanical models and application to the Lepontine Dome in the Central Alps. J. Metamorph. Geol. 23 (2), 75–95.
Cheloni, Daniele, D'Agostino, Nicola, Selvaggi, Giulio, 2014. Interseismic coupling, seismic potential, and earthquake recurrence on the southern front of the Eastern Alps (NE Italy). J. Geophys. Res., Solid Earth 119 (5), 4448–4468.
Chen, Wang-Ping, Yang, Zhaohui, 2004. Earthquakes beneath the Himalayas and Tibet: evidence for strong lithospheric mantle. Science 304 (5679), 1949–1952.
Chen, Yen-Ling, Hung, Shu-Huei, Jiang, Juen-Shi, Chiao, Ling-Yun, 2016. Systematic correlations of the earthquake frequency–magnitude distribution with the deformation and mechanical regimes in the Taiwan orogen. Geophys. Res. Lett.
Corbi, Fabio, Herrendoerfer, Robert, Funiciello, Francesca, Van Dinther, Ylona, 2017. Controls of seismogenic zone width and subduction velocity on interplate seismicity: insights from analog and numerical models. Geophys. Res. Lett.
Dalguer, Luis A., 2012. Numerical algorithms for earthquake rupture dynamic modeling. In: The Mechanics of Faulting: From Laboratory to Real Earthquakes, pp. 93–124.
Davis, Dan, Suppe, John, Dahlen, F.A., 1983. Mechanics of fold-and-thrust belts and accretionary wedges. J. Geophys. Res., Solid Earth 88 (B2), 1153–1172.
Del Gaudio, P., Di Toro, G., Han, R., Hirose, T., Nielsen, S., Shimamoto, T., Cavallo, A., 2009. Frictional melting of peridotite and seismic slip. J. Geophys. Res., Solid Earth 114 (B6).
Den Hartog, S.A.M., Niemeijer, A.R., Spiers, C.J., 2012. New constraints on megathrust slip stability under subduction zone P–T conditions. Earth Planet. Sci. Lett. 353, 240–252.
Di Toro, Giulio, Han, Raehee, Hirose, Takehiro, De Paola, Nicola, Nielsen, Stefan, Mizoguchi, Kazuo, Ferri, Fabio, Cocco, Massimo, Shimamoto, Tosihiko, 2011. Fault lubrication during earthquakes. Nature 471 (7339), 494–498.
Doglioni, C., Barba, S., Carminati, E., Riguzzi, F., 2011. Role of the brittle–ductile transition on fault activation. Phys. Earth Planet. Inter. 184 (3), 160–171.
Doglioni, C., Carminati, E., Petricca, P., Riguzzi, F., 2015. Normal fault earthquakes or graviquakes. Sci. Rep. 5.
Faccenda, Manuele, Gerya, Taras V., Chakraborty, Sumit, 2008. Styles of post-subduction collisional orogeny: influence of convergence velocity, crustal rheology and radiogenic heat production. Lithos 103 (1), 257–287.
Fisher, Ronald Aylmer, 1950. Contributions to Mathematical Statistics.
Gardner, J.K., Knopoff, Leon, 1974. Is the sequence of earthquakes in Southern California, with aftershocks removed, Poissonian? Bull. Seismol. Soc. Am. 64 (5), 1363–1367.
Gerya, Taras V., Yuen, David A., 2003. Characteristics-based marker-in-cell method with conservative finite-differences schemes for modeling geological flows with strongly variable transport properties. Phys. Earth Planet. Inter. 140 (4), 293–318.
Gerya, Taras V., Yuen, David A., 2007. Robust characteristics method for modelling multiphase visco-elasto-plastic thermo-mechanical problems. Phys. Earth Planet. Inter. 163 (1), 83–105.
Grenerczy, Gyula, Sella, Giovanni, Stein, Seth, Kenyeres, Ambrus, 2005. Tectonic implications of the GPS velocity field in the northern Adriatic region. Geophys. Res. Lett. 32 (16).
Gulia, Laura, Wiemer, Stefan, 2010. The influence of tectonic regimes on the earthquake size distribution: a case study for Italy. Geophys. Res. Lett. 37 (10).
Gutenberg, Beno, Richter, Charles F., 1944. Frequency of earthquakes in California. Bull. Seismol. Soc. Am. 34 (4), 185–188.
Hanks, Thomas C., Kanamori, Hiroo, 1979. A moment magnitude scale. J. Geophys. Res. 84 (B5), 2348–2350.
Heuret, Arnauld, Lallemand, Serge, Funiciello, Francesca, Piromallo, Claudia, Faccenna, Claudio, 2011. Physical characteristics of subduction interface type seismogenic zones revisited. Geochem. Geophys. Geosyst. 12 (1).
Jackson, James, 2002. Faulting, flow, and the strength of the continental lithosphere. Int. Geol. Rev. 44 (1), 39–61.
Kamer, Yavor, Hiemer, Stefan, 2015. Data-driven spatial b value estimation with applications to California seismicity: to b or not to b. J. Geophys. Res., Solid Earth 120 (7), 5191–5214.
Lapusta, N., Barbot, S., 2012. Models of earthquakes and aseismic slip based on laboratory-derived rate and state friction laws. In: The Mechanics of Faulting: From Laboratory to Real Earthquakes, pp. 153–207.
Maggi, Alessia, Jackson, J.A., Mckenzie, Dan, Priestley, Keith, 2000. Earthquake focal depths, effective elastic thickness, and the strength of the continental lithosphere. Geology 28 (6), 495–498.
Marzocchi, Warner, Sandri, Laura, 2003. A review and new insights on the estimation of the b-value and its uncertainty. Ann. Geophys.
Marzocchi, W., Sandri, L., Heuret, A., Funiciello, F., 2016. Where giant earthquakes may come. J. Geophys. Res., Solid Earth 121 (10), 7322–7336.
McCaffrey, Robert, 2008. Global frequency of magnitude 9 earthquakes. Geology 36 (3), 263–266.
Molnar, Peter, 1979. Earthquake recurrence intervals and plate tectonics. Bull. Seismol. Soc. Am. 69 (1), 115–133.
Nishikawa, Tomoaki, Ide, Satoshi, 2014. Earthquake size distribution in subduction zones linked to slab buoyancy. Nat. Geosci. 7 (12), 904–908.
Pasquale, V., Chiozzi, P., Verdoya, M., 2010. Tectonothermal processes and mechanical strength in a recent orogenic belt: Northern Apennines. J. Geophys. Res., Solid Earth 115 (B3).

Ranalli, Giorgio, 1995. Rheology of the Earth. Springer.
Rudnick, Roberta L., Fountain, David M., 1995. Nature and composition of the continental crust: a lower crustal perspective. Rev. Geophys. 33 (3), 267–309.
Schmeling, H., Babeyko, A.Y., Enns, A., Faccenna, C., Funiciello, F., Gerya, T., Golabek, G.J., Grigull, S., Kaus, B.J.P., Morra, G., et al., 2008. A benchmark comparison of spontaneous subduction models—towards a free surface. Phys. Earth Planet. Inter. 171 (1), 198–223.
Scholz, Christopher H., 2002. The Mechanics of Earthquakes and Faulting. Cambridge University Press.
Scholz, Christopher H., 2015. On the stress dependence of the earthquake b value. Geophys. Res. Lett. 42 (5), 1399–1402.
Schorlemmer, Danijel, Wiemer, Stefan, Wyss, Max, 2005. Variations in earthquake-size distribution across different stress regimes. Nature 437 (7058), 539–542.
Schultz, R.A., 1995. Limits on strength and deformation properties of jointed basaltic rock masses. Rock Mech. Rock Eng. 28 (1), 1–15.
Scordilis, E.M., 2006. Empirical global relations converting M S and m b to moment magnitude. J. Seismol. 10 (2), 225–236.
Seno, Tetsuzo, 2009. Determination of the pore fluid pressure ratio at seismogenic megathrusts in subduction zones: implications for strength of asperities and Andean-type mountain building. J. Geophys. Res., Solid Earth 114 (B5).
Singh, Chandrani, Singh, Arun, Chadha, R.K., 2009. Fractal and b-value mapping in Eastern Himalaya and Southern Tibet. Bull. Seismol. Soc. Am. 99 (6), 3529–3533.
Spada, M., Tormann, T., Wiemer, S., Enescu, B., 2013. Generic dependence of the frequency-size distribution of earthquakes on depth and its relation to the strength profile of the crust. Geophys. Res. Lett. 40 (4), 709–714.
Tatar, Mohammad, Hatzfeld, Denis, Martinod, Joseph, Walpersdorf, Andrea, Ghafori-Ashtiany, Mohsen, Chéry, Jean, 2002. The present-day deformation of the central Zagros from GPS measurements. Geophys. Res. Lett. 29 (19).
Tinti, Stefano, Mulargia, Francesco, 1987. Confidence intervals of b values for grouped magnitudes. Bull. Seismol. Soc. Am. 77 (6), 2125–2134.
Turcotte, D.L., Schubert, G., 2002. Geodynamics. Cambridge University Press.
Utsu, Tokuji, 1966. A statistical significance test of the difference in b-value between two earthquake groups. J. Phys. Earth 14 (2), 37–40.
van Dinther, Y., Gerya, T.V., Dalguer, L.A., Corbi, F., Funiciello, F., Mai, Paul Martin, 2013a. The seismic cycle at subduction thrusts: 2. Dynamic implications of geodynamic simulations validated with laboratory models. J. Geophys. Res., Solid Earth 118 (4), 1502–1525.
van Dinther, Y., Gerya, T.V., Dalguer, L.A., Mai, Paul Martin, Morra, G., Giardini, D., 2013b. The seismic cycle at subduction thrusts: insights from seismo-thermo-mechanical models. J. Geophys. Res., Solid Earth 118 (12), 6183–6202.
van Dinther, Y., Mai, Paul Martin, Dalguer, L.A., Gerya, T.V., 2014. Modeling the seismic cycle in subduction zones: the role and spatiotemporal occurrence of off-megathrust earthquakes. Geophys. Res. Lett. 41 (4), 1194–1201.
Wang, Qi, Zhang, Pei-Zhen, Freymueller, Jeffrey T., Bilham, Roger, Larson, Kristine M., Lai, Xi'an, You, Xinzhao, Niu, Zhijun, Wu, Jianchun, Li, Yanxin, et al., 2001. Present-day crustal deformation in China constrained by global positioning system measurements. Science 294 (5542), 574–577.
Wells, Donald L., Coppersmith, Kevin J., 1994. New empirical relationships among magnitude, rupture length, rupture width, rupture area, and surface displacement. Bull. Seismol. Soc. Am. 84 (4), 974–1002.
Wiemer, Stefan, 2001. A software package to analyze seismicity: ZMAP. Seismol. Res. Lett. 72 (3), 373–382.
Wiemer, Stefan, Giardini, Domenico, Fäh, Donat, Deichmann, Nicholas, Sellami, Souad, 2009. Probabilistic seismic hazard assessment of Switzerland: best estimates and uncertainties. J. Seismol. 13 (4), 449.